1.6 Measurement of Absolute Quantum Detection Efficiency of Reference Detectors

1.6.1 Absolute Calibration of Reference Detectors with Undispersed Synchrotron Radiation

1.6.1.1 Methodology

The absolute calibration of the reference standards–detectors used for ACIS quantum efficiency measurements–was performed using the Physikalisch-Technische Bundesanstalt (PTB) laboratory in the BESSY electron storage ring. Undispersed synchrotron radiation was used as the primary flux standard. Using the XSPEC fitting routine, a response matrix, constrained by spectral response measurements at MIT, was convolved with the known incident spectrum. The CCD gate structure parameters were then adjusted to minimize the χ^2 measure of fit. The quality of the resulting quantum efficiency model hinges on the accuracy of our knowing the synchrotron radiation. The spectral flux can be calculated with relative errors below 1% from the physical geometry of the detector with respect to the orbital plane of the electrons and other storage ring parameters: electron energy, ring current and magnetic field of the bending magnets [8].

Figure 1.57 illustrates the experimental set-up at the PTB laboratory. A standard MIT vacuum chamber, modified to hold two CCDs simultaneously was mounted to the PTB beamline via a ceramic electro-isolator to eliminate electrical interference between the CCD electronics and the BESSY facility. A gate valve and turbo pump located between the CCDs and the storage ring allowed the chamber to be connected and pumped down to the requisite vacuum without compromising the integrity of the storage ring. The CCDs were operated at the nominal flight temperature of -120 C°.

Even with just a single electron in the storage ring, the incident photon flux would have caused significant pileup (defined as multiple photons landing in the same pixel or neighboring pixels during one integration time) in the CCDs and corrupted the absolute calibration. Two measures were taken to reduce the flux to an acceptable level. First, a chopper wheel with a 2.00% transmission cycle was inserted into the beam line to reduce the incident flux. Second, only 256 rows of the CCD were read out. This readout mode reduced the integration time by a factor of four. The storage ring was usually operated with currents between 10 and 30 electrons, although measurements with as few as 5 electrons and as many as 50 electrons were performed to determine pileup effects.

The process of reading out 256 rows of the CCD limited the amount of the detector that could be calibrated during one measurement. To ensure that all the incident photons would fall on an active area of the detector (a necessary requirement for the determination of absolute quantum efficiency) a five mm high aperture was placed in the beam line and carefully centered on the electron orbital plane. The five mm slit produced an illumination pattern 208 pixels tall, and the CCD columns were nominally aligned perpendicular to the orbital plane. A two dimensional translation stage was incorporated into the section of the PTB beamline that the MIT chamber mounted to. To calibrate an entire chip, the chamber was moved an appropriate distance in the y direction, a 256-row swath of the CCD was read out, and the image was visually inspected to check that all the photons hit the active area. This procedure was repeated four or five times to calibrate the entire chip. The chamber was then moved in the horizontal direction to illuminate a second CCD inside the chamber. By placing two chips inside the chamber, the overhead associated with thermally cycling the CCD, venting the chamber, switching CCDs, re-evacuating the chamber and finally cooling the CCDs was eliminated. This configuration allowed calibration of as many as four chips in a single 48 hour user shift.

Given a well located electron beam, the synchrotron radiation from a storage ring can be derived from Schwinger's equation [11, 12]:

$$E(\lambda)^{SR} = E^{SR,\parallel}(\lambda) + E^{SR,\perp}(\lambda) = \frac{2e\rho^2 I}{3\varepsilon_0 \lambda^4 \gamma^4 a d^{SR}} \left\{ \int_{\psi_0-\psi'}^{\psi_0+\psi'} [1+(\gamma\psi)^2]^2 K^2_{\frac{2}{3}}(\xi)\,d\psi + \int_{\psi_0-\psi'}^{\psi_0+\psi'} [1+(\gamma\psi)^2]^2 (\gamma\psi)^2 K^2_{\frac{1}{3}}(\xi)\,d\psi \right\} \quad (1.20)$$

with

$$\gamma = \frac{W}{m_0 c^2}, \qquad \xi = \frac{2\pi}{3\gamma^3\lambda}[1+(\gamma\psi)^2]^{\frac{2}{3}}, \qquad \rho = \frac{W}{ecB}, \qquad \psi' = \frac{a}{2d^{SR}}$$

W, e and m_0 are the energy, charge and rest mass of the electrons and I is the current of the electrons in the storage ring. B is the magnetic induction of the bending magnets tangent to the observation point. a is the measure of the height of the beam, d^{SR} is the distance from the beam to the observation point, and ψ is the opening angle between the orbital plane and the observation point. c and ε_0 are fundamental constants, and K_x is the modified Bessel function, order x, of the the second kind. Thus, the spectral photon flux can be expressed in terms of seven measurable quantities:

$$\Phi_E = \Phi_E(E; W, B, I, \Sigma_y, d^{SR}, a, \psi) \quad (1.21)$$

where Σ_y characterizes the vertical position and divergence of the electrons at the observation point and the other quantities are the same as above. W and B were measured once for each run, and I was monitored continually. Horizontal variation of Φ_E is less than 10^{-3} over the width of the CCD [11]. Due to its dependence on the opening angle ψ, Φ_E varies strongly as the observation point moves out of the orbital plane of the electrons. Figure 1.58 shows how the BESSY spectrum softens as the height above the orbital plane increases. The calculated Φ_E is for one electron in the storage ring with no chopper wheel. For typical integration times and ring currents, no flux above 4 keV was detected by the CCDs.

Similar measurements were also performed using the PTB Wavelength Shifter (WLS) beamline. Additional magnets are introduced into the normal storage ring configuration, thus boosting the energy of the electrons and shifting the energy of the synchrotron radiation. Figure 1.58 also shows how the WLS spectrum changes as a function of height above the orbital plane. Although the spectrum extends beyond 20 keV, the low high energy quantum efficiency of the devices limits the detection of photons to below 14 keV. The WLS experiments will be discussed in greater detail in Section 1.6.1.3.

1.6.1.2 Analysis

Before discussing how to reduce the BESSY data, we review the assumptions that go into generating the CCD response function. The spectral redistribution function (or matrix) contains all the information (e.g. gain, fluorescence and escape peak amplitudes, FWHM vs. energy) necessary to perform modeling of a pulseheight distribution. Refer to Section 1.1 for a full description of the relevant quantities and their determination. The tool that generates the redistribution matrix (hereafter RM) is `rspgen`, written by A. Rasmussen [15]. `rspgen` uses a description of the CCD's response to monochromatic X-ray sources over a range of energies. Table 1.25 lists the options used to create RMs for the analysis of BESSY data.

When invoked, the unity command normalizes all redistribution function to unity at each energy. This is equivalent to assuming the branching ratios are not a function of energy. Although this is generally incorrect, by limiting the analysis to a specific energy range (0.3−4 keV) and to a particular subset of events (ASCA grades 0,2,3,4,6), the assumption is valid. The threshold values are matched to those used in the extraction of events from the CCD output. Although the same CCD/electronics combination was used for the BESSY calibration, the energy scale and noise conditions can vary slightly between the two measurements. The gain, offset, and broadening options account for the differences in the operating conditions and modifies the RM accordingly.

Option	Flag	Units	Remarks
unity	u	N/A	assumes unity branching ratios
split threshold	p	ADU	standard MIT values; depends on CCD electronics
event threshold	v	ADU	standard MIT values; depends on CCD electronics
grid spacing	E	keV	defines the energy grid that `rspgen` uses
gain	g	N/A	scales the ECD data
offset	o	ADU	offsets the ECD data
broadening	b	ADU	decreases or increases the ECD in quadrature
tailing	t	N/A	scales the low energy redistribution

Table 1.25: Summary of Adjustments to *rspgen* required for BESSY data

The purpose of the BESSY experiments is to obtain an absolute calibration for the reference detectors. This goal is achieved by multiplying a model of the CCD quantum efficiency with the RM, convolving the model response with the input spectrum, and comparing the results to the data. The parameters of the CCD QE model are adjusted to the find the best fit to the data. The current CCD model is the Slab and Stop Model synthesized by K. Gendreau [14]. It approximates the gate structure as piecewise-uniform layers of Si, SiO_2, and Si_3N_4 and the channel stop as layers of Si and SiO_2 with finite width. The final two CCD parameters are the width of the pixel and the depletion depth. The model assumes that the gate and channel stop are dead, and only those photons interacting in the depleted silicon will be detected.

Fitting the BESSY data with this model does not constrain all the parameters. The channel stops occupy a small area compared to the gate structure. This reduces the role of the channel stop parameters on the overall fit and leads to degeneracy in these three best-fit parameters[3]. Rather than determining these dimensions from BESSY data, we have measured the channel stops by other methods and frozen the parameters at these values. For the energy range of the White Light calibrations (E $<$ 4 keV), the quantum efficiency is mainly determined by the gate parameters and is insensitive to the depletion depth. Therefore, this parameter is also frozen at a value determined by another method (see Section 1.6.2 for details). Table 1.26 gives the parameters names, describes it and states whether or not it is fixed.

Parameter Name	Description	Status
Dead	Si gate thickness	free
SiOx	SiO_2 gate thickness	free
SiNit	Si_3N_4 gate thickness	free
Depl	Depletion depth	frozen–determined by branching ratio method†
CSWidth	Channel Stop width	frozen–determined by SEM measurements‡
CSSiOx	SiO_2 stop thickness	frozen–determined by SEM measurements‡
CSSi	Si p^+ thickness	frozen–determined by mesh experiments‡
Pix	Pixel width	frozen at 24 μm

†: see Section 1.6.2

‡: see Section 1.5

Table 1.26: CCD Model Parameters for BESSY absolute measurements

[3]Equally good χ^2 values can be achieved for a range of channel stops widths and thicknesses. The gate thicknesses and overall normalizations change with the values of the channel stop parameters used.

A total of eleven devices were characterized at BESSY during six separate 48 hour shifts[4]. Table 1.27 shows when each CCD was calibrated, how many data sets were taken, and the number of CCD positions illuminated. A typical measurement consisted of acquiring 2000 frames. Integration times ranged from 0.83−1.53 seconds, depending on which readout electronics were used. Storage ring currents ranged from 2 to 50 electrons, but typically the ring current was adjusted to either 10 or 20 electrons (again, this depended on readout electronics) in order to provide 350 counts/frame/quadrant. For a typical measurement, this yields on order of 3×10^6 counts in the 0.3−4.0 keV band over the illuminated part of the CCD.

Reduction of the data begins by extracting events from the raw data and saving the location, pulse-height value, and frame number of each event in an event list. The storage ring current is monitored by the BESSY facility, and this data stream is searched for the loss of electrons from the storage ring during our measurements. If such a loss occurred, the event list is temporal filtered. Pileup effects are very dependent on the initial flux rate, and limiting the data to a single ring current allows the most accurate correction. Finally, the event list is further filtered by event grade selection and a `XSPEC` compatible PHA file is produced. At this time, the data from an entire quadrant is averaged together in a 5mm $\times$ 6mm spatial bin.

The `rspgen`-generated RM, an "atable" model of the incident synchrotron radiation spectrum, the CCD model, and the PHA file are loaded into `XSPEC`. The atable model (*/usr/acis/atable/bessy_new.mod*) has two parameters, an overall normalization factor and another parameter that exists for historical reasons but is no longer used. The data is rebinned, the energy range limited to 0.3-4.0 keV and the model parameters are left free or frozen according to Table 1.26. If pileup is significant, two techniques are available to correct the data. One method developed by A. Rasmussen utilizes a mtable model that is compatable with `XSPEC`. This empirical model simulates the effects of pileup from BESSY data and relies on the incident flux levels being sufficiently low [16]. It has one phenomenological parameter that corresponds to the incident flux rate. `XSPEC` then fits for gate thicknesses, the source normalization and the pileup parameter. The other method developed by S. Jones (see Section 1.4) utilizes extensive laboratory data from incident flux–count rate linearity studies. The pulse-height spectrum is directly corrected, and this corrected PHA file is then read directly into `XSPEC`.

Figure 1.59, Figure 1.60, and Figure 1.61 show the best fit models with the data for individual quadrants of detectors w190c3, w190c1, and w103c4. The RMs used for the fit can

[4]The last measurement were done on Wavelength Shifter beamline.

be found in:

/ohno/d9/mjp/BESSY/XSPEC/w190c3/t0852/c1.rsp
/ohno/d9/mjp/BESSY/XSPEC/w190c1/t2347/tmp_memo.rsp
/ohno/d9/mjp/BESSY/XSPEC/w103c4/t1414/tmp_c1.rsp

Pileup corrections have been applied to the data for all three devices. The Rasmussen method was used for devices w190c1 and w190c3, while the Jones method was used for w103c4. To check the consistency of each method, w190c3 was also corrected using the Jones method. Normalization values from the two techniques differed by $\sim 0.1\%$, indicating excellent agreement between the two correction methods. Table 1.28 shows the best-fit parameters, the RMS error, and the normalization accuracy for each reference detector as well as listing the values of the frozen parameters.

As a whole, the model fits for detectors w190c1 and w190c3 are quite good. In both cases the data:model ratio shows two deviation from unity: a narrow feature around 1.8 keV and a systematic underestimation of the flux above 2.2 keV. An underestimation of the Si Kα fluorescence could help contribute to the narrow feature. Analysis of the response function data indicates that the fluorescence yields in the current response matrices are too low (see Section 1.14). Another probable source of error is the use of the Henke optical constants. Our EXAFS measurements (see Section 1.6.4) show large deviations from the tabluated Henke values around both the O Kα and S Kα absorption edges. In the future we will incorporate these optical constant measurements in our model. The excess above 2.2 keV results from the good, but not exact, correction for pileup. The best-fit normalizations are within 1% of the calculated value, but could change with an improved pileup algorithm and inclusion of more accurate fluorescence data. Another measure of the goodness of fit for these two devices is the comparison of the derived gate thicknesses. w190c1 and w190c3 came from the same wafer, and hence, underwent the exact same fabrication process. The differences between the derived thickness for the Si, SiO_2, and Si_3N_4 layers are well within the errors.

The fit for reference detector w103c4 is noticeably worse than the other two devices. The RMS error is higher, and the best-fit normalization is nearly 6% too low. Above 2 keV, the model underestimates the data by almost 10%. The deviation from unity illustrates the importance of correcting the data for pileup. At the same time, however, the best-fit values for the three gate layers are reliable. Studies with devices w190c1 and w190c3 indicate that neglecting pileup influences the RMS error and normalization but has only small effects on the best-fit gate thicknesses. This behavior is consistent with the low level pileup model discussed in Section 1.4. To first order, pileup shifts events out of the acceptable grades (this explains the low best-fit normalization) and deposits some small fraction of these events' charge into non-physical, higher energy events (this accounts for the excess of counts above 2 keV).

Extensive measurements at MIT CSR have shown that the QE of front-illuminated CCDs have little spatial variation over bin sizes of 0.77 mm^2. Because the intensity and shape of the BESSY spectrum changes over the illumination pattern, similar measures of fine spatial uniformity are non-trivial. Our current spectral fitting procedure is to integrate all the data into 5mm $\times$ 6mm spatial bins. Table 1.29 shows the average counting rate (cts/sec/e^- ring current) normalized to the y001 position for each quadrant of w103c4 at five different CCD positions. Data is from the August 95 shift. The counting rates for y768 are expected to be higher than those for any other quadrants since the beam current was lower for this measurement and pileup effects should be smaller. Statistical errors for the data sets are less than 0.002. Finally, on average there is one bad column per quadrant that does not extend the length of the CCD. This analysis does not account for the reduction of the active area caused by the bad column, and this introduces an uncertainty on order of 0.004 to the ratios.

A final check of the BESSY data is a comparison of the relative quantum efficiency measurements made at MIT CSR. Reference standards w190c3 and w103c4 were calibrated with respect to one another at discrete energies using the HEXS (see Section 1.7.1 for details). The model fitting to the BESSY data yields absolute efficiencies for both devices. Dividing these continuous curves by one another provides an independent check of both the MIT CSR measurements and the quality of the CCD model. The upper panel of Figure 1.62 shows the absolute quantum efficiencies determined from the synchrotron data. The higher efficiency of w103c4 is easily understood as it has a thinner gate oxide layer than w190c3. The bottom panel of Figure 1.62 shows the discrete relative measurements made at MIT CSR *vs.* the continuous BESSY-derived relative quantum efficiencies. The errors associated with the MIT CSR values are systematic and currently estimated at 2%[5].

1.6.1.3 Preliminary Assessment of Wavelength Shifter Data

The measurements made during the December 96 user shift were performed with the PTB Wavelength Shifter (WLS) beamline. With the incident radiation going well beyond 15 keV, it was hoped the measurements would extend the absolute calibration of the reference standards up to the high energy limit of the AXAF observatory. Another goal of this measurement was to provide an independent determination of the depletion depths. Unlike the White Light beamline which can only constrain the low energy quantum efficiency dominated by the gate thicknesses, the harder spectra of the WLS beamline produces photons that easily transverse the length of depleted silicon–the requisite condition to accurately model the high energy quantum efficiency and the depletion depth.

Initial analysis of the WLS data reveals two potential problems with the quality of the data. Reduced data products indicate that the electronics were performing sub-optimally during half of the measurements. The problems can be simply characterized as a spatial and temporal variation in the bias levels [18]. Techniques do exist to correct for such effects, but it is unclear how well they will work. It was known that the WLS would produce many more photons than the White Light beam for a given ring current. Anticipating problems with pileup, the storage ring currents were reduced from typical White Light operating conditions by at least a factor of two. Unfortunately, the extent that pileup influences high

[5]Statistical errors for these data are negligible.

energy spectra has only recently been fully appreciated. Given the way the BESSY data was collected, it is quite possible that the data may prove difficult to accurately correct for pileup [6]. Initial `XSPEC` fitting indicate that pileup is much more severe than for the White Light data.

[6]The beating of the chopper wheel with the readout time of the CCDs leads to different pileup conditions for some fraction of the data [17].

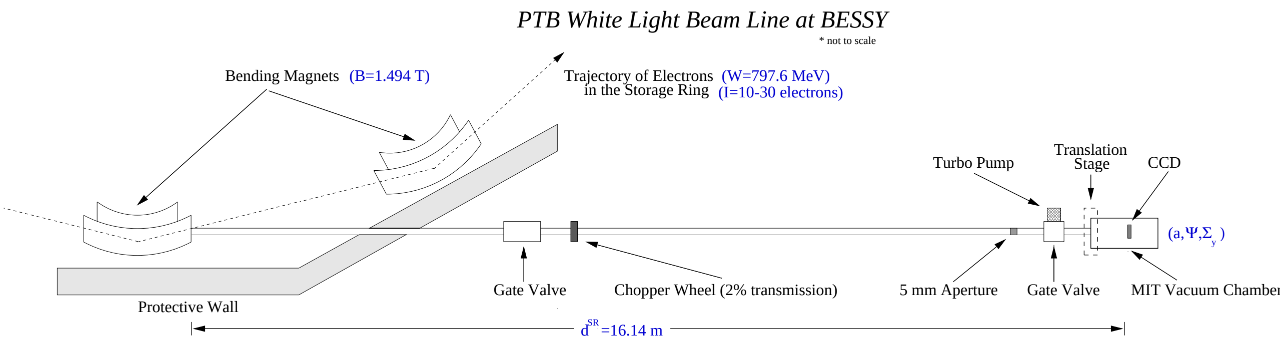

Figure 1.57: Sketch of the PTB laboratory

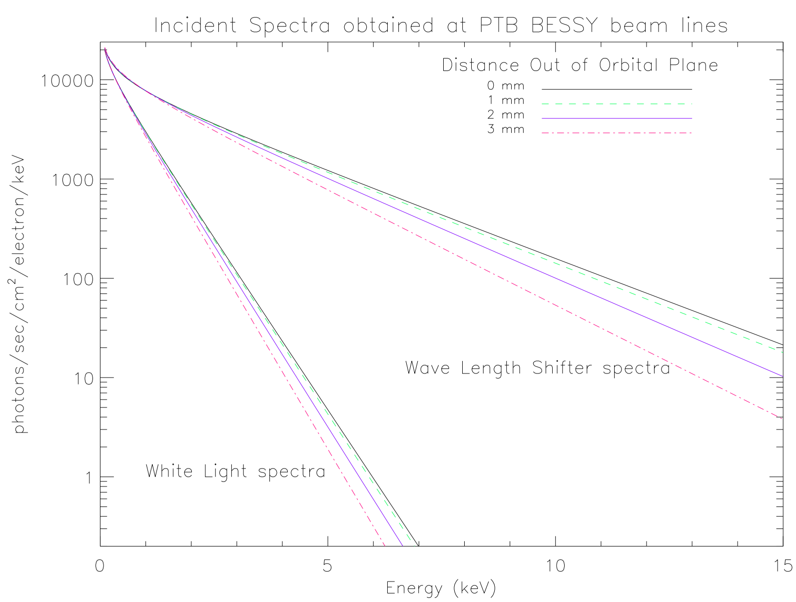

Figure 1.58: White Light and WLS BESSY spectra as a function of height above the orb ital plane

Chip	**Date**	**Data Sets**	**Chip Positions**	**Electronics**
w34c3	Mar 95	7	4	acis 3
w34c3	Apr 95	17	4	acis 3
w34c3	May 95	6	5	acis 6
w34c3	Aug 95	3	1	acis 3
w103c1	Mar 95	7	4	acis 3
w102c3	May 95	6	5	acis 6
w103c2	May 95	5	5	acis 6
w103c4	May 95	6	5	acis 6
w103c4	Aug 95	5	5	acis 3
w147c3 (BI)	Aug 95	15	5	acis 3
w148c4 (BI)‡	Aug 95	6	5	acis 3
w190c1	Jun 96	10	5	dea-sn014
w190c1	Dec 96†	6	5	dea-sn017
w190c3	Jun 96	10	5	dea-sn014
w168c2	Dec 96†	5	5	dea-sn017
w203c2	Dec 96†	19	5	dea-sn017

†: Wavelength Shifter Measurement
‡: ACIS-2C device

Table 1.27: Summary of synchrotron measurements made with PTB beamlines at BESSY.

	CCD Parameters (in μm)							(0.3-4 keV)	
	Free			Fixed				RMS	
							Depletion	Deviation	Best Fit
Chip	Si†	SiO_2‡	Si_3N_4	CS Si	CS SiO_2	CS Width	Depth	of Fit	Normalization
w190c3	0.259	0.354	0.031	0.35	0.45	4.1	71.3	2.54%	$1.000 \pm .003$
w190c1	0.261	0.358	0.029	0.35	0.45	4.1	70.6	2.24%	$0.994 \pm .003$
w103c4	0.291	0.202	0.030	0.35	0.45	4.1	57.9	3.88%	$0.956 \pm .003$

†: typical 90% confidence error is ± 0.008 μm
‡: typical 90% confidence error is ± 0.011 μm

Table 1.28: CCD model parameter fit results from synchrotron radiation measurements

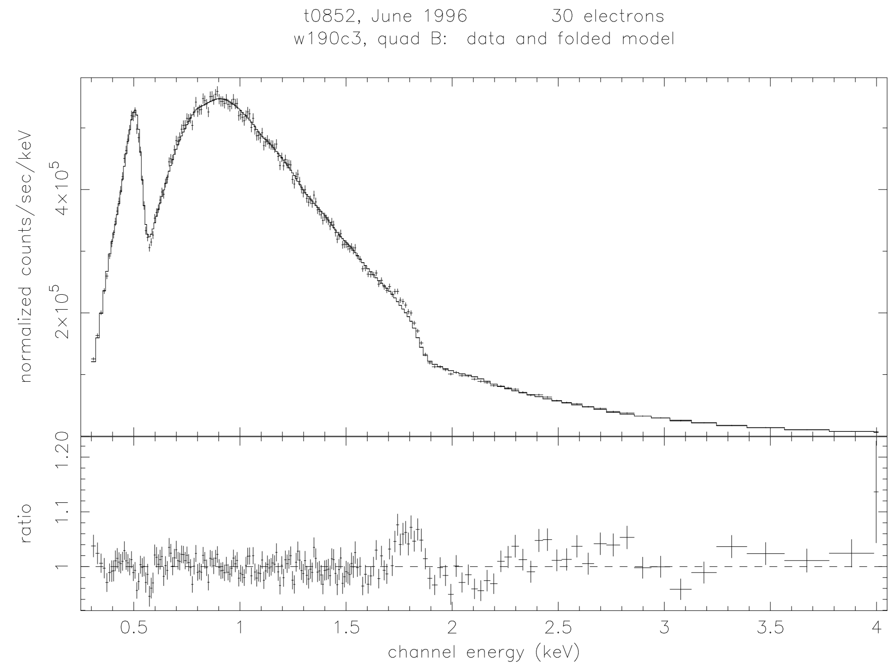

Figure 1.59: w190c3, quad B: BESSY data vs. model

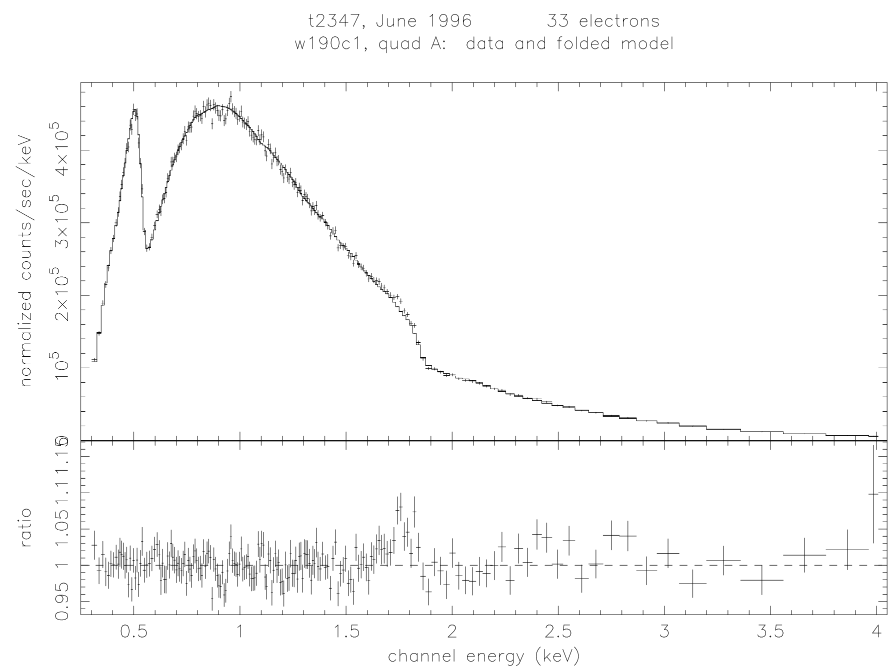

Figure 1.60: w190c1,quad A: BESSY data vs. model

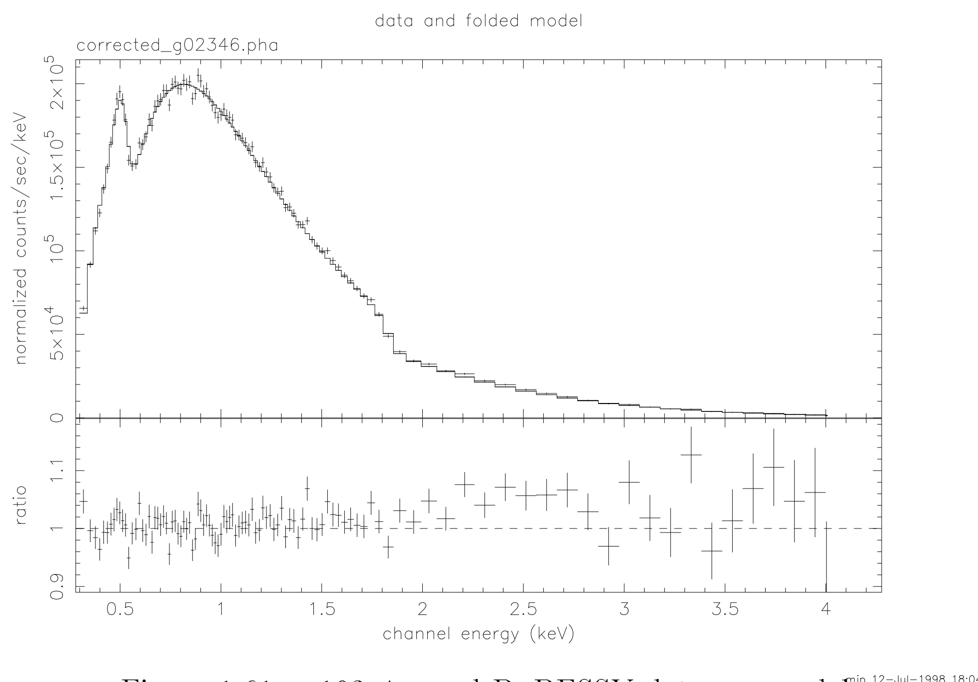

Figure 1.61: w103c4, quad B: BESSY data vs. model

CCD Position	Ring Current	Quad A	Quad B	Quad C	Quad D
y001	19 e^-	1.0000	1.0000	1.0000	1.0000
y209	19 e^-	1.0069	1.0087	1.0056	1.0049
y417	19 e^-	1.0069	1.0062	1.0080	1.0025
y625	19 e^-	1.0031	1.0050	1.0043	0.99938
y768	18 e^-	1.0056	1.0019	1.0025	1.0012

Table 1.29: Average counting rate (cts/sec/e^- ring current) for w103c4 normalized to CCD position y001. Statistical errors for all measurements are below .002. No pileup corrections have been applied.

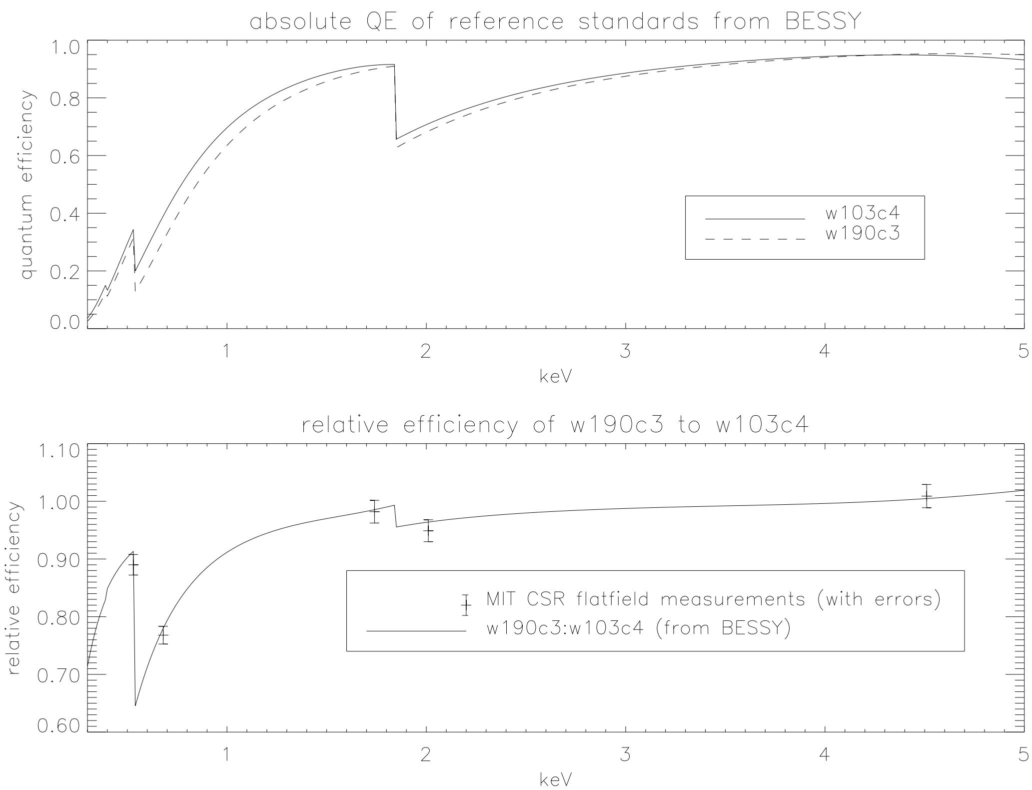

Figure 1.62: BESSY absolute efficiencies vs. MIT CSR relative efficiencies for reference detectors w190c3 and w103c4.

1.6.2 High-Energy Quantum Efficiency from Grade Branching Ratios

1.6.2.1 Introduction

In a number of ACIS memos issued by K. Gendreau and G. Prigozhin some years ago numerous techniques were suggested for determining a depletion depth of a CCD. All of the suggested techniques were very complicated and not too accurate. Described here is the most simple, efficient and stable technique. It is not sensitive to the way the events are counted (for example, reasonably small changes in thresholds do not affect the result), does not require any assumptions about the potential profile, and, probably, the most important, depletion depth can be extracted from just one dataset of Fe^{55} data (no need to step through the range of voltages, for instance).

1.6.2.2 Description of the technique

This technique makes use of the following idea. Let us assume that CCD is illuminated with a monochromatic source of X-ray photons whose characteristic absorption length λ is

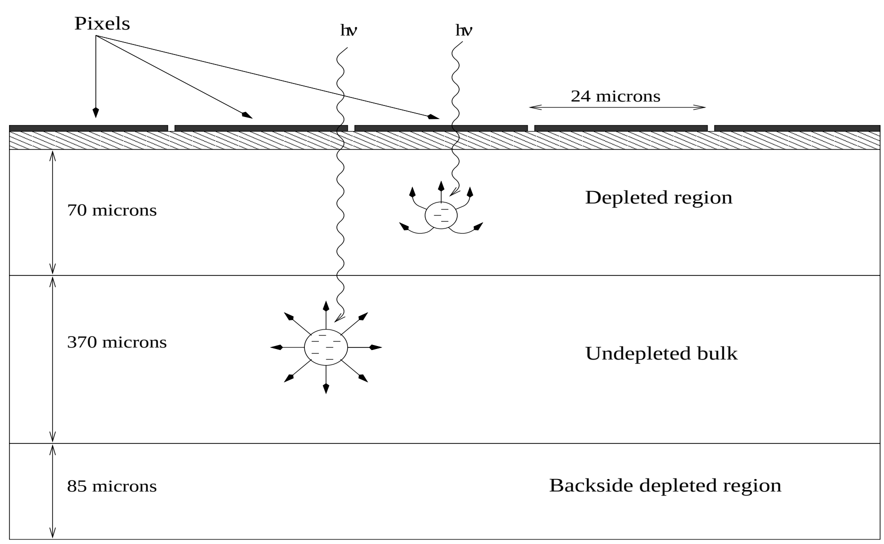

Figure 1.63: Schematic of the CCD depleted layers.

smaller than, but comparable to the depletion depth. If an interaction of the photon with Si occurres in the depleted region of the CCD, the created electron cloud will be drawn into the potential wells by the electric field and all the charge will be collected (see Fig. 1.63).

Depending on where relative to pixel boundaries the photon landed the resulting event can be either a single-pixel or a split one (can be either horizontally or vertically split, or grade 6), but the sum of the amplitudes of the pixels containing a signal charge should account for all the charge generated by the photon, and, hence, be part of the main peak in the response histogram. On the other hand, if an interaction occurred in an undepleted bulk of the semiconductor, the charge cloud diffuses more or less uniformly in all directions. Part of the cloud drifting towards the back side of the device will be lost. Electrons moving towards the front surface enter the depletion region and being pulled by an electric field end up in the potential wells of the CCD. Due to initial diffusion of charge the registered event in this case is a widespread multipixel cloud. According to the ASCA grading scheme this is a grade 7 event and, since part of the initial charge is lost to the backside junction, the amplitude is lower than the peak energy even if all the pixels of the event are summed together.

If we denote N_d the number of interactions in the depleted region and N_{und} the number of events in the undepleted bulk, then, due to exponential distribution of the of the number of interacting photons as as a function of depth, a simple equation holds (see Fig. 1.64 for a better understanding):

$$N_{und} = (N_d + N_{und}) \exp(-\frac{d_d}{\lambda}) \tag{1.22}$$

where d_d is the depletion depth of the device.

This implies the following algorithm of the depletion depth calculation.

1. Sum the the intensities of the grades 0,1,2,3,4,6 and determine what is the number of events N_d in the main peak. Find the peak center E_c and width σ, and then count how many events are within the $\pm 3\sigma$ interval from the peak center.

2. Count what is the total number of events N_{und} in the grade 7 below $E_c - 3\sigma$.

3. Calculate the depletion depth d_d according to the formula derived from (1.22):

$$d_d = \lambda \ln(\frac{N_d}{N_{und}} + 1) \tag{1.23}$$

The logarithmic function in the above equation makes the result very insensitive to small changes in both N_d and N_{und} caused by statistical uncertainties or, say, choosing different set of grades for the peak counts calculation. At the same time, small changes of the depletion depth cause changes in the N_d and N_{und} to go in the opposite directions (because the sum $N_d + N_{und} = const$, see Fig. 1.64), thus amplifying the change in the result. Sharp sensitivity of the result to the changes of the depletion depth has been confirmed by experiment where the gate voltage was stepped from 0 to +10 Volts.

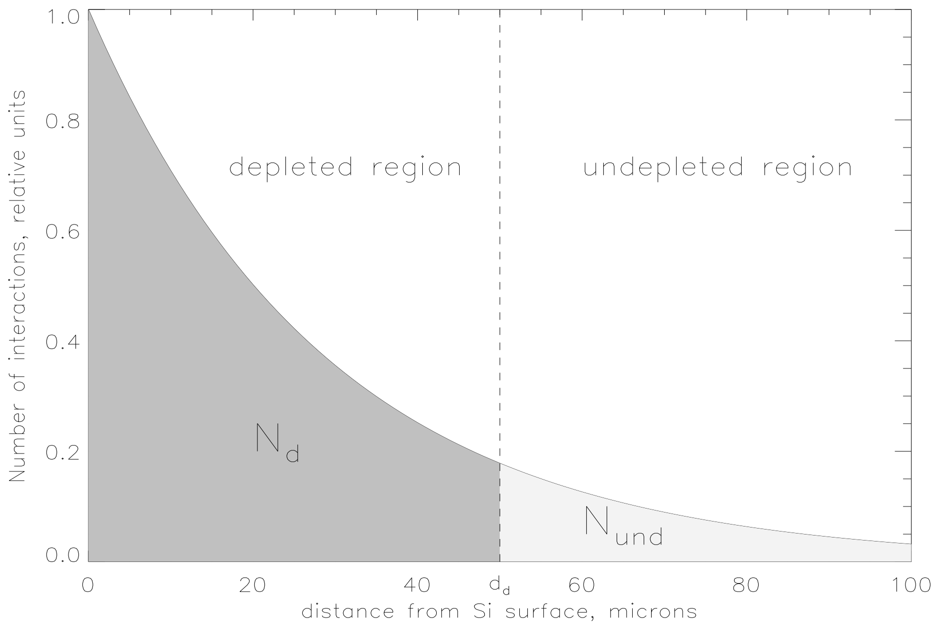

Figure 1.64: Exponential distribution of the number of interacting photons as a function of distance from the surface.

1.6.2.3 A typical example and possible sources of errors

a. Statistical errors

Here is an exemplary calculation of depletion depth for the ACIS flight device $w193c2$. The dataset */ohno/di/database/w193c2/butthead/fe55/30nov96/1713/* represents 416 frames of Fe^{55} X-rays taken in Butthead at -120^o C with standard imaging array voltages of +1 and +11 Volts. The average count rate is 1110 $counts/sector/frame$. The calculation is made for the chip sector 2.

In Fig. 1.65 is shown a standard set of histograms of different grades. The number of counts in the K_α peak of combined grades 0 1 2 3 4 6 histogram within the $\pm 3\sigma$ interval is 355719 ± 596 (an error is calculated as a square root of number of counts). The number of counts in grade 7 histogram below $E_c - 3\sigma$ is 33092 ± 182 (again assuming an error being the square root although, strictly speaking, it may not be the right estimate because this is not the gaussian distribution). This results in the depletion depth of 70.9 microns. Assuming the worst case of statistical errors going in the opposite directions we get the limits for d_d from 70.69 to 71.07 microns, which means that the statistical accuracy for the standard dataset is better than 0.3%.

b. K_β line induced error

There is a source of systematic error associated with the nonmonochromatic nature of the Fe^{55} radioactive source. Presence of the K_β line in the spectrum leads to underestimation of the depletion depth because the characteristic absorption length at 6.4 keV ($\lambda_\beta = 38.0$ microns) is bigger than at 5.89 keV ($\lambda_\alpha = 28.77$ microns) and, hence, K_β line produces a larger share of events in the undepleted bulk. To calculate the error introduced by the K_β line let us rewrite equation (1.22) separately for both lines:

$$N_{und\alpha} = (N_{d\alpha} + N_{und\alpha}) \exp(-\frac{d_d}{\lambda_\alpha}) \quad (1.24)$$

$$N_{und\beta} = (N_{d\beta} + N_{und\beta}) \exp(-\frac{d_d}{\lambda_\beta}) \quad (1.25)$$

Quantities $N_{d\alpha}$ and $N_{d\beta}$ can be determined from the experimental data as the number of counts in each of the corresponding peaks, whereas $N_{und\alpha}$ and $N_{und\beta}$ cannot be separated. But, since the sum $N_{und\alpha} + N_{und\beta}$ is known (it is number of counts in the grade 7 tail), equations (1.24) and (1.25) can be solved numerically after transforming them into the following:

$$\frac{N_{d\alpha}}{exp(\frac{d_d}{\lambda_\alpha}) - 1} + \frac{N_{d\beta}}{exp(\frac{d_d}{\lambda_\beta}) - 1} - (N_{und\alpha} + N_{und\beta}) = 0 \quad (1.26)$$

The Newton-Rafson method was implemented to solve (1.26). For the above example (number of counts in the K_β peak equals 45709) the corrected solution gives $d_d = 73.8$ microns, or, 4% increase of d_d.

c. Pileup

One other source of error can be pileup. It throws events out of the main peak into events with higher amplitude. The most simple first order correction would be to assume that all the events in the pileup peak (located at the energy $2E_c$) originates from two main peak photons landed on the top of each other, and that the "high energy tail" of grade 7 distribution (events to the right from the K_β peak) comes from one main peak photon and one grade 7 event piled up together. After adding the corresponding number of counts to the main peak and to the grade 7, the corrected depletion depth (using formula (1.23)) becomes 69.64 microns.

d. Interactions beyond detection limit

Some photons interact so deep in the bulk of silicon that the portion of charge collected in one pixel is too small to be detected. An event will not be registered by the data analysis software if the charge in each pixel falls below the event threshold. To determine the distance from the depletion region border beyond which the charge will stay undetected.

S. Jones' code was used to implement the solution of diffusion equation as described in the Hopkinson's paper [20]. The solid line on Fig. 1.66 shows charge collected in the pixel for 5.89 keV photon stopped in the field free region as a function of distance from the cloud center to the depletion region boundary. A dotted line in the plot shows the same thing calculated on the simple assumption that charge diffuses uniformly in all directions. This approach is attractive since the result can be expressed by a single analytical formula. In this case charge Q_{pix} collected in one pixel is proportional to the solid angle under which the pixel is seen from the center of the cloud. Solving the stereometry quiz in the case of cloud center located at the pixel center line results in the following:

$$Q_{pix} = \frac{Q_{tot}}{4\pi}(8\arcsin\sqrt{\frac{2{d_c}^2 + a^2}{4{d_c}^2 + a^2}} - 2\pi) \qquad (1.27)$$

where a is a pixel size, d_c is the distance from the center of the charge cloud to the depletion region border, Q_{tot} is total electron charge created by the photon. As expected, both curves in Fig. 1.66 converge at large distances, when the influence of the boundary becomes negligible. At small d_c simplified approach results in the collected charge approximately factor of 2 smaller than the full solution, which also makes sense. In the middle range of distances smaller than 140 microns, though, the difference is surprisingly big to justify the use of the simple approach.

For the data analyzed above the event threshold is 38 ADU, or, multiplied by gain, 35 electrons. From the above plot (solid line) one can determine critical distance $d_c = 59$ microns beyond which a photon is not detected. It means that 1.1% of all the events stay undetected (the ones that are deeper than $70.9 + 59$ microns from surface) instead of being counted as grade 7 events.

In order to calculate the correction for the depletion depth introduced by the undetected photons the equation (1.22) should be modified into

$$N_{und} + N_{lost} = (N_d + N_{und} + N_{lost})\exp(-\frac{d_d}{\lambda}) \qquad (1.28)$$

and supplemented by a similar equation for the region beyond the depletion boundary:

$$N_{lost} = (N_{und} + N_{lost})\exp(-\frac{d_c}{\lambda}) \qquad (1.29)$$

where we introduced N_{lost} – number of interactions beyond the detection border located at the distance $d_d + d_c$ from the silicon surface.

These two equations can be converted into the corrected formula for the depletion depth

$$d_d = \lambda\ln(\frac{N_d}{N_{und}(\frac{1}{1-\exp(-\frac{d_c}{\lambda})})} + 1) \qquad (1.30)$$

For the above analyzed example the corrected depletion depth according to (1.30) is 67.3 microns, which constitutes a 5% correction. It is clear from this analysis that reducing the event threshold will significantly improve the accuracy of the original formula (1.23).

e. Simultaneous correction for both K_β and undetected photons

It is possible to apply the formalism developed above to describe simulteneously both mechanisms that distort the result of the measurement. In order to do that, equations (1.28) and (1.29) have to be written separately for the K_α and K_β lines. Notice that the critical distance d_c from the depleted layer boundary is different at different energies and we need to use two parameters $d_{c\alpha}$ and $d_{c\beta}$ instead. Combining the following four equations together:

$$N_{und\alpha} + N_{lost\alpha} = (N_{d\alpha} + N_{und\alpha} + N_{lost\alpha}) \exp(-\frac{d_d}{\lambda_\alpha}) \quad (1.31)$$

$$N_{lost\alpha} = (N_{und\alpha} + N_{lost\alpha}) \exp(-\frac{d_{c\alpha}}{\lambda_\alpha}) \quad (1.32)$$

$$N_{und\beta} + N_{lost\beta} = (N_{d\beta} + N_{und\beta} + N_{lost\beta}) \exp(-\frac{d_d}{\lambda_\beta}) \quad (1.33)$$

$$N_{lost\beta} = (N_{und\beta} + N_{lost\beta}) \exp(-\frac{d_{c\beta}}{\lambda_\beta}) \quad (1.34)$$

one can arrive to the equation somewhat similar to (1.26):

$$N_{d\alpha} \frac{1 - exp(-\frac{d_{c\alpha}}{\lambda_\alpha})}{exp(\frac{d_d}{\lambda_\alpha}) - 1} + N_{d\beta} \frac{1 - exp(-\frac{d_{c\beta}}{\lambda_\beta})}{exp(\frac{d_d}{\lambda_\beta}) - 1} - (N_{und\alpha} + N_{und\beta}) = 0 \quad (1.35)$$

The C program *~gyp/het/dep_Kbeta_corrected* implements the Newton-Rafson method to solve (1.35) numerically for d_d when other parameters are known.

f. Summary of error estimates

The conclusion is that statistical errors for the depletion depth determination using standard set of Fe^{55} frames are negligible (less than 0.3%). The biggest sources of systematic errors are K_β line photons and photons interacting deep in the bulk of the silicon. Corrections from those two factors go in the opposite directions and tend to compensate each other because the K_β photons increase number of events counted as grade 7, whereas undetected ones diminish this number. For the analyzed example they almost entirely cancelled each other, although, undetected photons seem to pull d_d down a little stronger. As a result, a calculation made with the simple formula (1.23) seems to overestimate depletion depth by about 2% due to pileup and the detection limit. To get a more accurate result a very detailed modeling is necessary.

1.6.2.4 Results for the flight devices.

The technique described above was applied to all frontside illuminated flight devices. Depletion depths were extracted from the Fe^{55} data sets taken at the HIREFS spectrometer chamber. These data have lower flux rate than other chambers, and, hence, very low level of pileup. The computation of the depletion depth included correction for the presence of the K_β line in the source spectrum as well as correction for the undetected photons according to equation (1.35). No pileup correction was made because the level of pileup in these data is low. Results are summarized in Table 1.30.

Device	Location	Depletion Depth, μm								Remarks
		Φ PI = +2,+10V (standard)				Φ PI = -5,+5V (reduced dark current)				
		c0	c1	c2	c3	c0	c1	c2	c3	
w203c4r	I0	66.4	66.9	66.8	66.4	47.6	48.1	48.0	48.7	
w193c2	I1	67.4	66.5	67.8	66.6	48.3	47.4	47.5	47.9	
w158c4r	I2	66.8	67.2	66.5	66.3	47.7	47.9	47.8	47.4	
w215c2r	I3	66.1	67.3	66.5	66.2	48.7	47.8	48.5	47.9	
w168c4r	S0	64.8	65.5	65.5	65.3	44.9	45.8	45.5	45.4	
w182c4r	S2	79.5	79.1	80.6	79.9	57.7	58.2	58.1	58.3	
w457c4	S4	73.3	74.2	73.9	73.6	53.4	53.5	53.0	53.4	
w201c3r	S5	73.0	74.4	74.7	74.4	52.1	53.4	52.9	53.2	
w198c1	ref.	73.7	73.9	74.7	72.8	52.3	51.6	52.2	51.3	
w461c4	ref.	81.2	81.3	80.2	80.6	59.2	58.9	58.2	58.4	
w203c2	ref.	68.1	68.1	67.0	67.2	48.0	49.0	48.9	47.8	

Table 1.30: Depletion Depth Estimated from 5.9 keV branching ratio

For standard image section voltages (+2,+10 Volts) every measurement was made at three different temperatures, namely, -130, -120, and -110 degrees C. Since depletion depths should not depend on temperature (at least in the narrow temperature range), for every quadrant of every chip the results were averaged over three measurements. Typical standard deviation of the result is 0.35 microns. As can be seen in Table 1.30, some of the chips show quadrant-to-quadrant variations of the depletion depth on the order of 1.5 microns. Such variations exceed statistical error and, most likely, are real and caused by nonuniformity of the substrate resistivity. They translate into approximately 2% variations of QE at 8.4 keV and provide an explanation why spatial variation of QE at this energy is much larger than at lower energies.

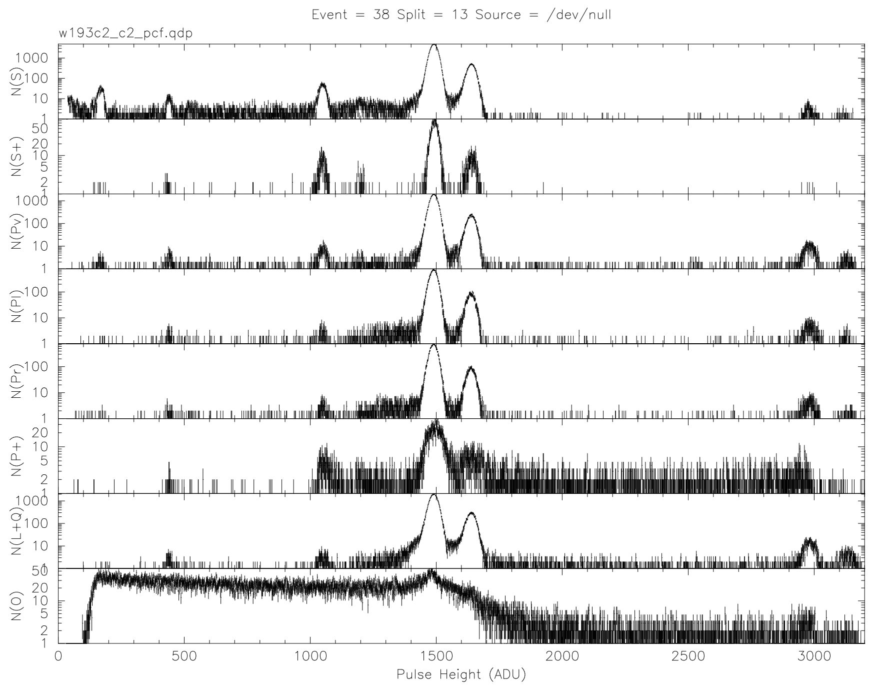

Figure 1.65: Histograms of different grades for Fe^{55} X-rays. Eight panels (from top to bottom) correspond to ASCA grades 0 through 7.

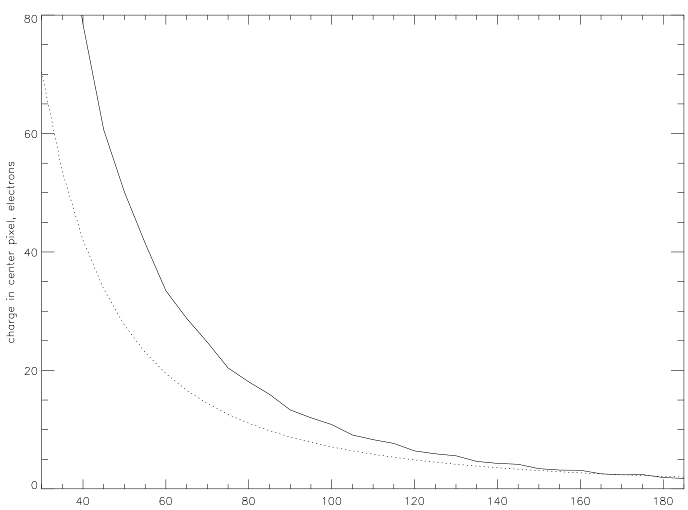

Figure 1.66: Charge collected in the center pixel from the Fe^{55} photon landing in the neutral bulk as a function of distance from depletion region boundary.

1.6.3 Comparison Betweeen Measured and Modeled Relative Quantum Efficiency at Energies above 5 keV

At energies above 4–5 keV quantum efficiency of the device depends entirely on the depletion depth. Consequently, the results of the depletion depth measurements described in Section 1.6.2 can be checked against the results of the quantum efficiency measurements of the flight devices relative to the reference chips. Since depletion depths were extracted from the data taken in the HIREFS chamber, the results of the two measurements are completely independent. Absolute QE numbers at two energies - 5.898 KeV (Manganese K_α line) and 8.047 keV (Copper K_α line) were calculated for both flight and reference devices based on the assumption that any photon interacting within the depleted layer will be detected. Table 1.6.3 shows the results of these calculations along with the results of the relative QE measurements in the big chambers. Both results are in good agreement.

Device	Loc.	Deplet. depth, μm	Absolute QE (calculated)		Relative QE (calculated)		Relative QE (measured)		Rel. QE difference (meas.-calc.)		Reference device
			5.9 keV	8.05 keV	5.9 keV	8.05 keV	5.9 keV	8.05 keV	5.9 keV	8.05 keV	
w203c4r	I0	64-65	0.875	0.594	1.039	1.086	1.031	1.106	-0.008	0.02	w103c4
w193c2	I1	64-65	0.875	0.594	1.039	1.086	1.033	1.087	-0.006	0.001	w103c4
w158c4r	I2	64-65	0.875	0.594	1.039	1.086	1.030	1.096	-0.009	0.01	w103c4
w215c2r	I3	64-65	0.871	0.588	0.974	0.94	0.986	0.932	0.012	-0.008	w190c3
w168c4r	S0	63-64	0.867	0.583	0.970	0.93	0.974	0.919	0.004	-0.011	w190c3
w182c4r	S2	75-76	0.905	0.646	1.07	1.18	1.068	1.211	-0.002	0.031	w103c4
w457c4	S4	70-72	0.894	0.626	1.00	1.00	1.000	1.003	0.000	0.003	w190c3
w201c3r	S5	71-72	0.894	0.626	1.00	1.00	1.001	1.008	0.001	0.008	w190c3
w103c4	ref	57	0.842	0.547							
w190c3	ref	71	0.894	0.626	1.062	1.145	1.058	1.164	-0.004	0.019	w103c4
mean									-0.0013	0.008	
σ									0.0066	0.014	

Table 1.31: Comparison of relative QE measured directly and calculated from the results of depletion depth measurement

1.6.4 Near edge structure of X-ray absorption in the CCD response

1.6.4.1 Introduction

In order to produce an accurate model of CCD quantum efficiency it is very important to know precisely the optical constants of the materials comprising the gate structure of the device. Widely used Henke data are quite inaccurate at energies close to the absorption edges. We undertook an effort to measure the transmission of the corresponding films in order to to fill in this gap.

The CCD gate structure contains three different materials: silicon dioxide, silicon nitride (Si_3N_4), and polycrystalline silicon, which is heavily doped with phosphorus. All the X-ray absorption edges of these materials, namely, silicon L (100 eV), nitrogen K (400 eV), oxygen K (532 eV), and silicon K (1840 eV) are within the range of interest for ACIS.

In the course of technology development for manufacturing backside CCD, Lincoln Lab implemented a technique for etching away the thick silicon substrate, leaving only a thin layer of material at the surface of the wafer. This technology turned out to be exceptionally well suited for making thin films supported by a rigid frame, allowing them to be handled easily. Usually, at low energies the transmission of a material is derived from the results of the measurement of total electron yield. With the Lincoln Lab technology it is possible to make extremely thin free standing films and measure transmission directly. We used synchrotron radiation to measure the transmission of these materials as a function of energy. There is no single beamline which can cover such a wide range of energies, and for this reason measurements were performed at three different synchrotrons.

1.6.4.2 Sample preparation

All the samples were prepared in a similar manner. A film was grown on the silicon substrate and then silicon from the back side of the wafer was etched away in a circular opening approximately 0.5 centimeter in diameter. The etching stops when the film is reached. This results in an extremely thin film sitting on the top of the silicon frame. The cross section of such structure is shown in Fig. 1.67.

The following samples were prepared at Lincoln Lab for the transmission measurements:
1. Thin SiO_2 film (dry oxidation of Si wafer at 1000^o C, a process identical to the one used for CCD gate oxide growth), nominally 0.14 microns thick.
2. Thick SiO_2 film (wet oxidation at 1000^o C, a process used for channel stop oxide growth), approximately 1.5 microns thick.
3. A sandwich of $SiO_2 + Si_3N_4 + SiO_2$, a copy of the CCD gate insulator structure, nominal thicknesses 0.06 + 0.03 + 0.015 microns.

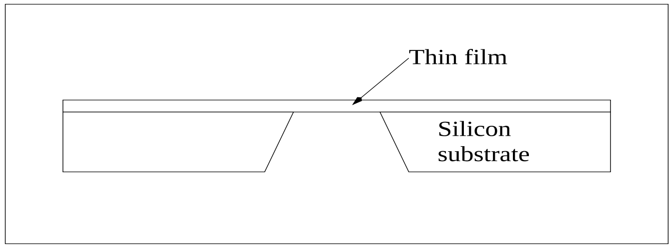

Figure 1.67: Cross section of the thin film sample.

4. Phosphorus doped polycrystalline silicon, 0.6 microns thick.
5. The same polycrystalline silicon film partially oxidized, nominally 0.46 + 0.2 microns of $Si + SiO_2$ respectively.

1.6.4.3 Measurement details

X-ray transmission measurements of samples 1 and 3 at low energies (60 eV – 900 eV) were performed at the Advanced Light Source (Lawrence Berkeley National Lab), beamline number 6.2.3, which is equipped with a grating monochromator with superb energy resolution (resolving power 7000). Three different gratings are needed to cover the entire energy range. For each grating the interval is further divided into two or three subranges due to the necessity of using different filters to suppress higher orders. For this reason a dataset for each sample consists of 8 separate subsets. It should be noted that changing of the grating requires realignment of the beam.

Only samples 1 and 3 were characterized at ALS. Three other samples were too thick for the measurement in this energy range, being opaque at energies below 300 – 400 eV and above the O K edge (SiO_2 sample). The energy step in the region from 360 to 580 eV containing nitrogen and oxygen edges was set to 0.25 eV, to 0.5 eV for energies below 180 eV (around the Si L edge), and 1 eV for the rest of the energy range.

Transmission at energies around the silicon K edge was measured at two other synchrotrons: at BESSY (Berlin) and at the Synchrotron Radiation Center (Madison, Wisconsin). The Canadian Double Crystal Beamline at the SRC has a double crystal monochromator with a resolution of 0.9 eV. It utilizes a pair of InSb(111) crystals (instead of the more commonly used in this range silicon), which is important for this measurement in order to avoid silicon edge "steps" in the incoming flux. Due to the low energy of electrons in the storage ring (800 MeV) and the double crystal arrangement of the monochromator, this beamline has very low higher order light penetration (below 0.2%). The data were taken in the range from 1770 to 2500 eV. The energy step was 0.25 eV around Si edge (from 1830 to 1860 eV), and 1 eV for the rest of the range. The accuracy and reproduceability of the SRC data is better than 0.1%, the noise being hardly noticeable.

At BESSY measurement were made over a wider range, from 1300 eV to 3000 eV. In general BESSY results are much noisier, but they are very valuable since they span a wider range and this helps to constrain the thickness of the films more reliably.

Since the X-ray flux emitted by a storage ring is continuously changing, it is necessary to normalize the output intensity to the input flux. This requires two detectors for any measurement - one in front, and one behind the sample. A solid state X-ray detector was installed downstream from the sample to register the output flux. At all three beamlines it was an uncovered Hamamatsu GaAsP photodiode G1127-02. Again, this was one of the precautions taken to avoid silicon absorption edges anywhere in the measurement system. Upstream from the sample a transparent beam normalization detector monitored the input flux. At ALS and BESSY this was a metal mesh whose electron yield was measured. At SRC a gas ionization chamber served as the beam normalization detector.

Each measurement consisted of two passes through the energy range – one with the sample in the beam, another one with the sample out. The ratio of the two normalized fluxes is the transmission of the film.

1.6.4.4 Measurement results.

a. Silicon L, nitrogen and oxygen K edges

In Fig. 1.68 the solid line shows the transmission of the thin SiO_2 film at energies below 800 eV. Very strong near-edge oscillations can be seen at energies above the silicon L and oxygen K absorption edges. In the areas where near-edge structure does not play a significant role, a fit to the standard Henke data was made with a thickness of the film as a free parameter. The best fit thickness was found to be 0.157 microns, and the corresponding transmission curve is shown on Fig. 1.68 as a dotted line. The deviation of the measured transmission from the Henke data is very strong above the absorption edges, and the edges themselves are shifted. The structure above 100 eV corresponds to silicon L_1, L_2, and L_3 edges at 158, 107, and 105 eV respectively. At the oxygen edge a very strong resonant absorption peak is found at 538 eV.

A transmission curve for the $SiO_2 + Si_3N_4 + SiO_2$ sandwich (which is an exact copy of the CCD gate isolator) is shown on the Fig. 1.69. In addition to the silicon and oxygen edges this plot shows a prominent nitrogen K edge, also shifted from the tabulated atomic value. The transmission of this sandwich was modeled as a combination of the Henke-derived Si_3N_4 transmission and the experimentally measured transmission of SiO_2. The best fit (thicknesses of both materials being free parameters) is shown in Fig. 1.69 as the dotted line.

b. Silicon K edge

Fig. 1.70 contains absorption curves (not transmission!) of polysilicon, SiO_2, and the $SiO_2 + Si_3N_4 + SiO_2$ sandwich in the close vicinity of the silicon K edge. Each sample shows a sharp resonant peak right above the edge. Due to chemical shifts each of the three materials exhibits the silicon K-edge at slightly different energy. For polysilicon the peak is at 1841 eV; for SiO_2 it is at 1847.3 eV. The $SiO_2 - Si_3N_4 - SiO_2$ sandwich shows two distinct peaks which, although are not well-resolved, can be determined to be at 1847.3 and 1844.7 eV. The first one can obviously be attributed to SiO_2, while the second one originates from Si_3N_4. Polysilicon absorption shows a lot of structure due to its crystalline and ordered nature, whereas silicon dioxide has fewer peaks because it is amorphous and uncorrelated interference from remote atoms smears out the features.

The difference between the edge and resonant peak energies of polysilicon and SiO_2 can be seen very nicely in the oxidized polysilicon sample transmission in Fig. 1.71. A dashed line in this plot represents the result of fitting to this data the product of the transmissions of the separate films of polysilicon and SiO_2. The quality of the fit is so good that the dashed line can hardly be seen under the solid line.

In order to fill a gap in the data (no measurements were made in the range from 900 to 1300 eV), and also to extend the results to higher energies, we used Henke data (which should be adequate at energies far enough from the edges).

For each of the materials standard Henke data were used to fit the transmission at energies below the edge and far above the edge, where the near edge oscillations become weak. This procedure allows us to define the thickness of each film. The results are slightly different from the nominal values and are reflected in the labels in the above Figures. The densities of the materials used for those calculations were 2.19, 2.33 and 3.44 g/cm^3 for SiO_2, polysilicon and Si_3N_4, respectively. For both polysilicon and SiO_2 near-edge measurements were combined with Henke atomic scattering factors for silicon and oxygen, and mass absorption coefficient were produced in the range from 60 eV to 15 keV.

We encountered some difficulties in our attempt to separate optical constants of the Si_3N_4 film from the other components of the sandwich, most likely due to deviations from stoichiometry in one or more constituent layers. Because of that, for further applications we used a transmission of the sandwich as a whole unit, instead of deriving a mass absorption coefficient for each component.

1.6.4.5 CCD quantum efficiency.

Having all the absorption coefficients in hand it is possible to calculate the quantum efficiency of the CCD taking into account transmission of all the layers in the gate structure of the frontside CCD. In this model we accounted for the overlaps between the gates of the CCD, and assumed triangular edges of the channel stop oxide layer (which is a good approximation for the so-called "bird's beak" shape of those edges). Thicknesses of the layers were taken from the results of Scanning Electron Microscope (SEM) measurement of a sibling device cross section (see Fig 1.46). In Fig. 1.72 is shown a plot of quantum efficiency as a function of energy for the frontside illuminated device. The dashed line in the Figure represents results of the quantum efficiency measurement of the frontside CCD at the SX700 beamline at BESSY. No fitting of the model to the data has been made for this plot. The deviation of the experimental points from the model at higher energies can be explained by the known second order light penetration of the SX700 monochromator at higher energies. In the analysis of the SX700 results the second order light counts are excluded in the CCD, while the reference photodiode cannot discriminate between orders. This results in the underestimation of the QE values for the CCD. It should also be mentioned that the above model accounts only for the transmission losses in all the layers (in great detail, though) and does not deal with the redistribution of counts into the low energy tail. This should not be a very significant factor for the frontside illuminated CCDs.

A similar plot for the backside illuminated device is shown in Fig. 1.73. Triangular points show the results of experimental measurements of the quantum efficiency of the backside illuminated device at the SX700 beamline at BESSY. The plot extends to very low energies around the silicon L edges, although the device loses its ability for spectral resolution below 250 eV. It still can be used for imaging, and its QE can be high enough, as can be seen from the Figure. The best agreement of experimental data with the transmission model was reached assuming a surface thickness of oxide layer of 0.055 microns, whereas the nominal thickness specified by Lincoln Lab is 0.035 microns. Besides that, we had to multiply the calculated QE by a factor of 0.96 to obtain an agreement with the experiment. This is expected, since for the backside devices a noticeable fraction of events is lost to the low energy tail. A more sophisticated model is necessary to account for this effect. As in the case with the frontside devices, a discrepancy at higher energies is attributed to second order light contamination.

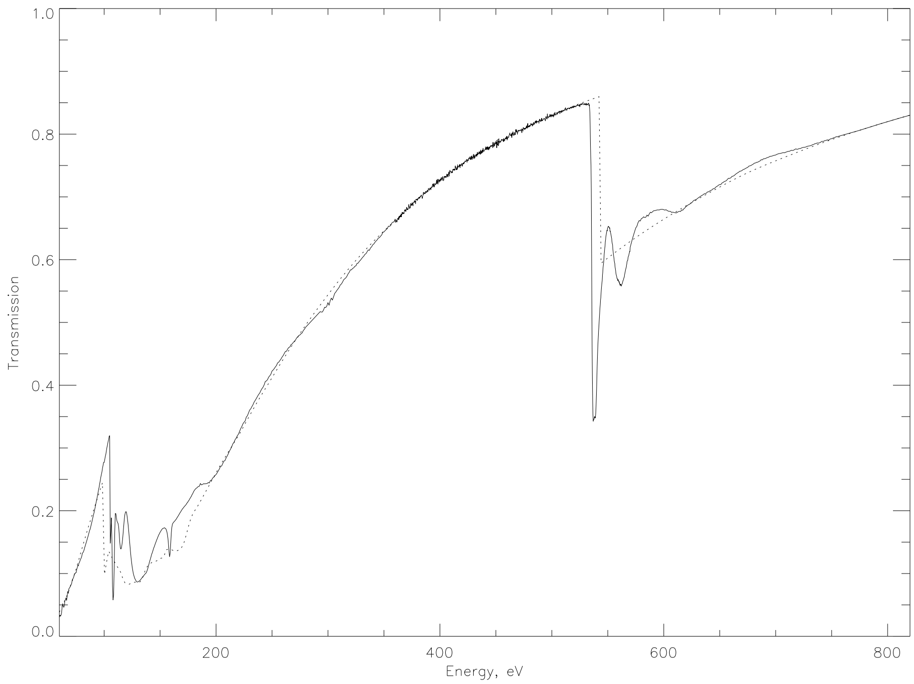

Figure 1.68: Transmission of the thin SiO_2 film as a function of energy (solid line). Dotted line represents standard Henke data.

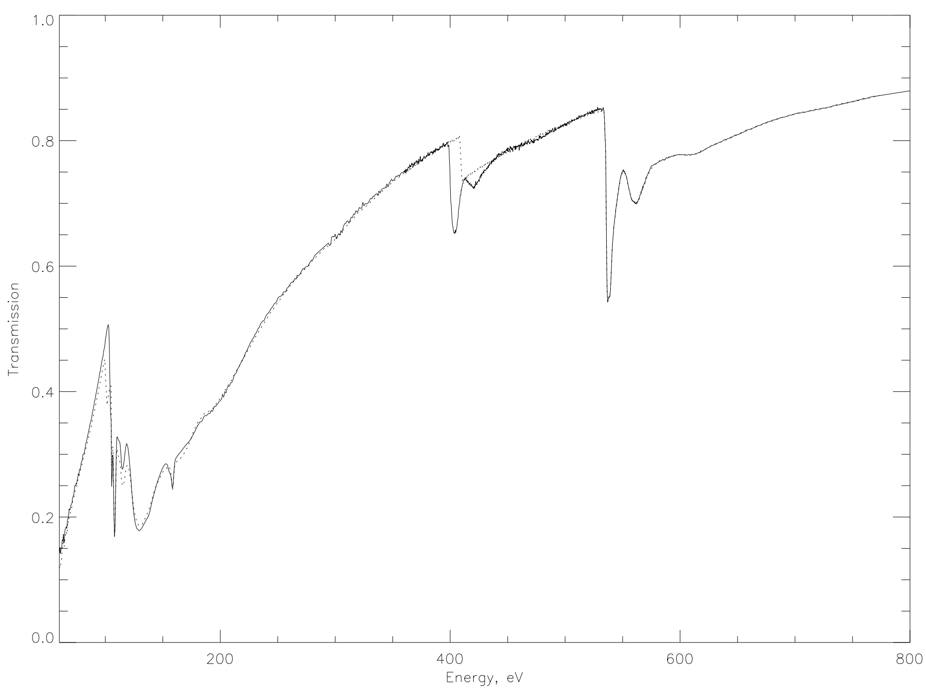

Figure 1.69: Transmission of the sandwich (solid line).

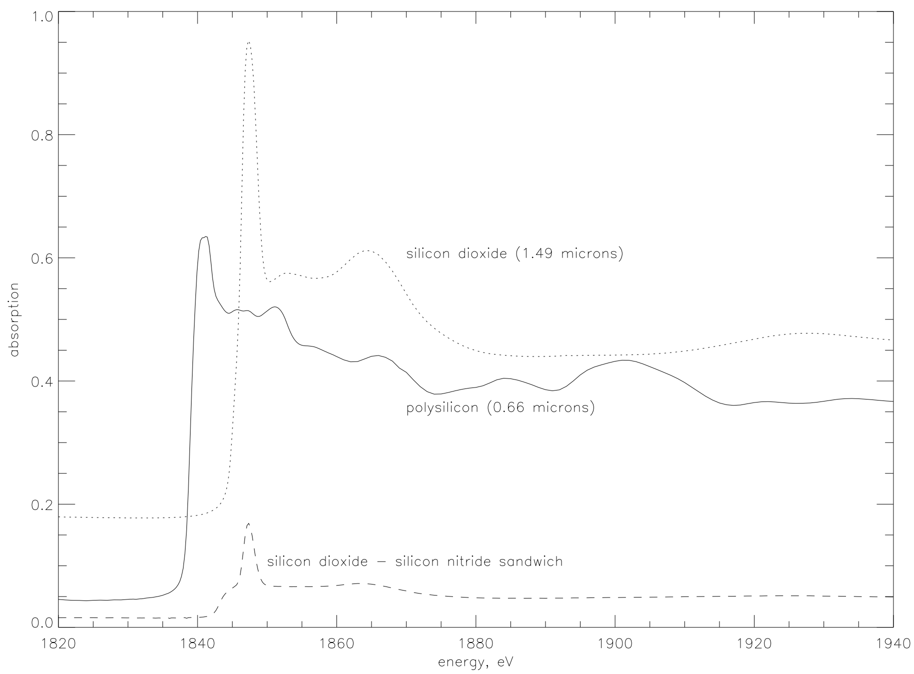

Figure 1.70: Absorption of the thin films of polysilicon (solid line), silicon dioxide (dotted line) , and $SiO_2 - Si_3N_4$ (dashed line) sandwich.

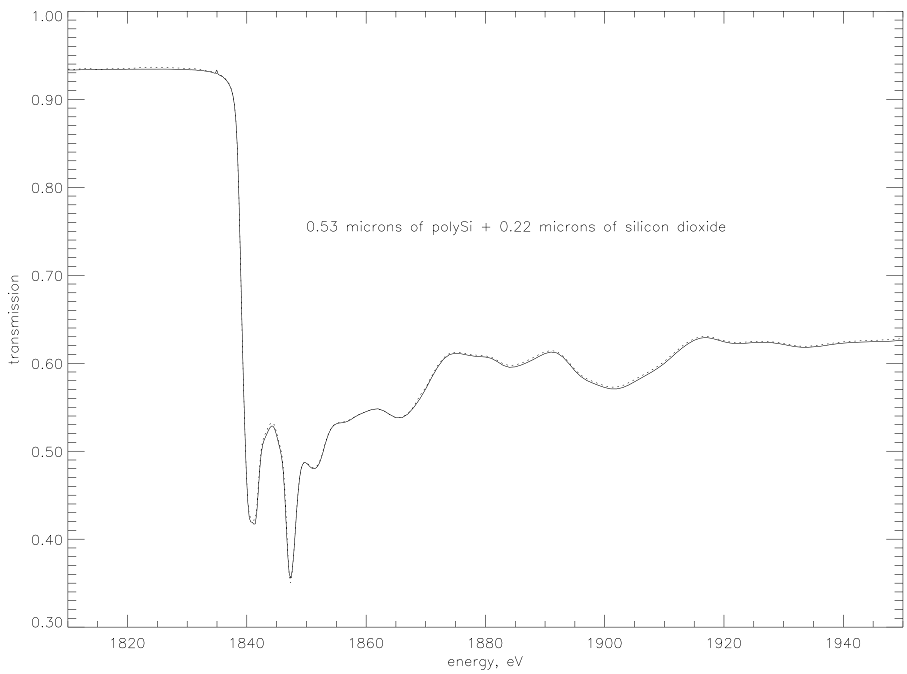

Figure 1.71: Transmission of the oxidized polysilicon film (solid line) and result of the best fit to it of the product of the polysilicon and SiO_2 transmissions (dotted line).

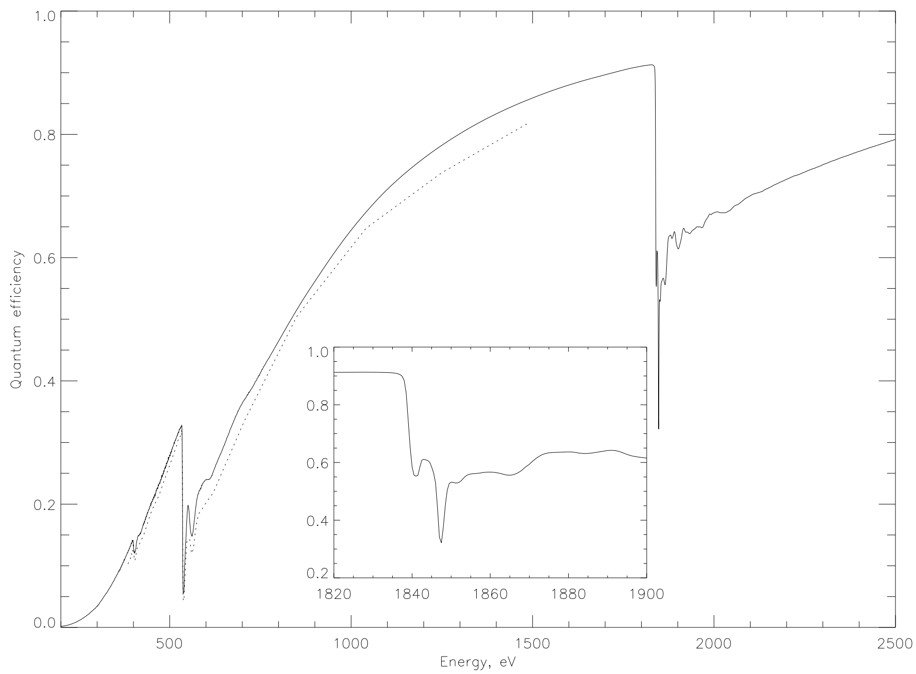

Figure 1.72: Quantum efficiency of the frontside illuminated CCD. Dashed line is the result of the QE measurement at SX700 line at BESSY.

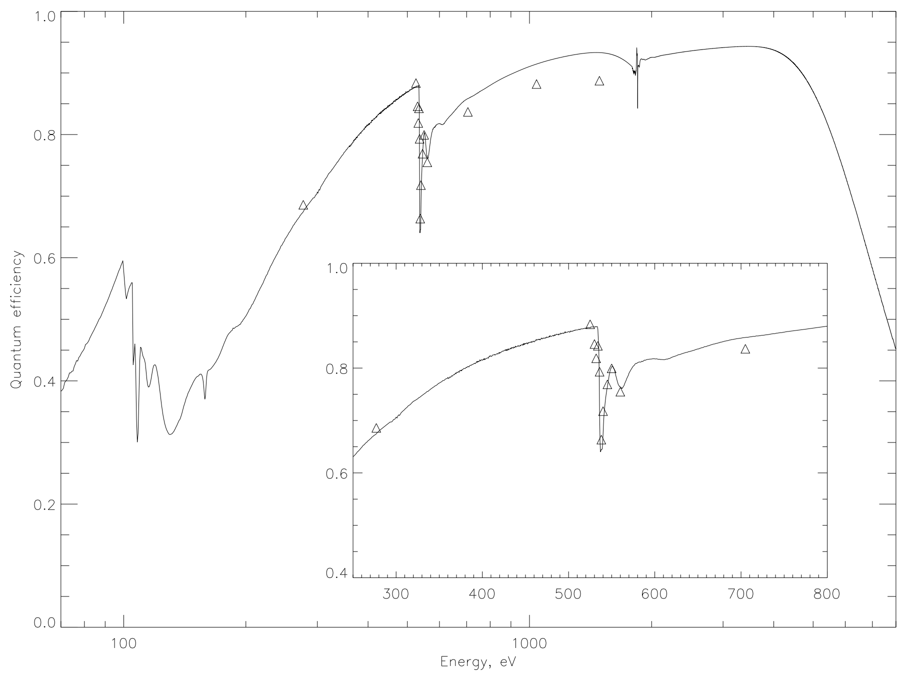

Figure 1.73: Quantum efficiency of the backside illuminated CCD. Triangles mark experimental results from SX700 at BESSY.

1.6.5 Validation of High Speed Tap Data Acquired at XRCF

1.6.5.1 Purpose

The purpose of this section is to show that the High Speed Tap event lists can be used to determine absolute quantum efficiency of the ACIS instrument.

1.6.5.2 The Data Set

During flat field calibration operations at the XRCF in May of 1997, telemetry data and High Speed Tap data were taken simultaneously for a number of sources for all ten of the flight devices.

The standard procedure was to begin a science run, then use the High Speed Tap to collect raw data frames for each of the chips being operated.

After some processing, the event list generated from the raw High Speed Tap data frames can be directly compared with the events telemetered by the flight software.

The data set chosen for this comparison is TRW ID I-IAS-EA-2.017. The chip is s4 (aka. w457c4). The anode is silicon. The data set was captured on 09 May 1997 at 22:12 GMT.

1.6.5.3 The Telemetry Data Processing

The telemetry event list is from Science Run 72, which began on 09 May 1997 at 17:48 GMT as TRW ID I-IAS-SG-2.008.

The parameter block used was xfaint_win_s.te. xfaint_win_s.te is full frame, faint telemetry, trickle bias, with a window.

The window block used was xsik56b50.2d. For the s4 chip, this has two windows. The first window begins at row 9 (counting from 0) and is 28 rows high. The second window begins at row 972 and is 28 rows high. All 1024 columns were telemetered.

The first event for the science run was on 09 May 1997 at 18:03 GMT. The last event for the science run was on 09 May 1997 at 23:49 GMT.

An ERV event list and fits format average bias frame for this science run were created from the ACIS telemetry using PSCI. For a description of PSCI and the ERV format see http://acis.mit.edu/ttools/psci.html.

The ERV format event list was converted to ACIS RV format using an IDL program which combines the fits format average bias file and the E RV format event list. For a description of the ACIS RV format see http://acis.mit.edu/ttools/acis-analysis.html.

To directly compare the telemetry event list with the High Speed Tap event list, events which the telemetry includes but the High Speed Tap does were removed. There are three types of events that the High Speed Tap event list does not include; events on quadrant boundaries, events taken before (22:17 GMT) or after (23:00 GMT) the High Speed Tap data were captured, and events in frames that the High Speed Tap dropped.

1.6.5.4 The High Speed Tap Data Processing

The High Speed Tap event list used was taken as TRW ID I-IAS-EA-2.017, which began on 09 May 1997 at 22:12 GMT. The first event was at 22:17 and the last event was at 23:00 GMT.

An RV format event list was created from the fits format bias frames (taken with the gate valve shut, immediately prior to the data) and the fits format data frames using "xrcf_find_events".

To directly compare the High Speed Tap event list to the telemetry event list the High Speed Tap times and coordinates were converted to telemetry times and coordinates, and events not included in the telemetry event list were removed.

The times had to be converted because the telemetry times are given in seconds from the beginning of 1997 while the High Speed Tap times are given in seconds from the beginning of 1994.

The coordinates needed to be converted because the telemetry row and column coordinates are given in chip coordinates while the High Speed Tap coordinates are given in readout coordinates.

There are two types of events that the High Speed Tap event list includes that the telemetry event list does not; events that occur outside of the telemetry window, and events in frames that the telemetry dropped.

1.6.5.5 Event List Comparison

Both of the event lists in the comparison contain events from 755 frames. The average number of events per frame in the 56 rows of the comparison is 56.6 events per frame. The total number of events in the filtered telemetry event list is 42738. There are 42768 events in the filtered High Speed Tap event list.

1.6.5.6 Spectral Resolution Comparison

After subtracting the average bias and delta-overclocks, the event amplitudes in the two event lists can be directly compared. The spectra for ACIS grade bit map 0x1d05 0x0047 0x0004 0x0047 0x1133 0x0003 0x1100 0x0000 0x1d04 0x0000 0x0004 0x0000 0x0000 0x0003 0x0000 0x0000 (ASCA grades 02346) for both the High Speed Tap and telemetry event lists are shown in Figure 1.74.

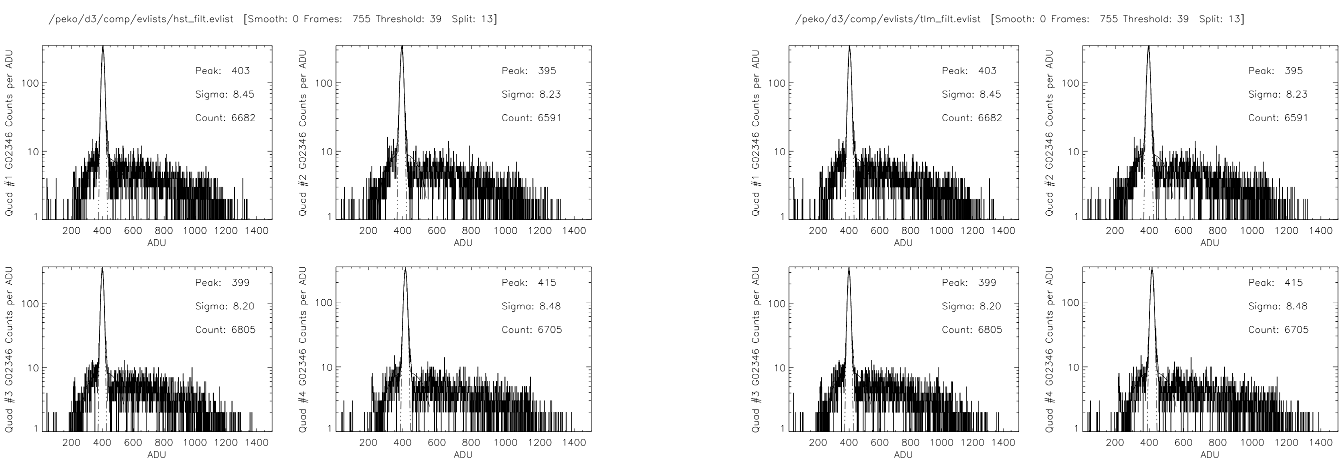

Figure 1.74: Telemetry and High Speed Tap Spectra

The peak and sigma fit to the data for each of the four quadrants is the same for each of the event lists.

1.6.5.7 Event Timing Comparison

The total number of events in each frame is shown in Figure 1.75 for both the telemetry event list and the High Speed Tap event list as well as the difference between the two.

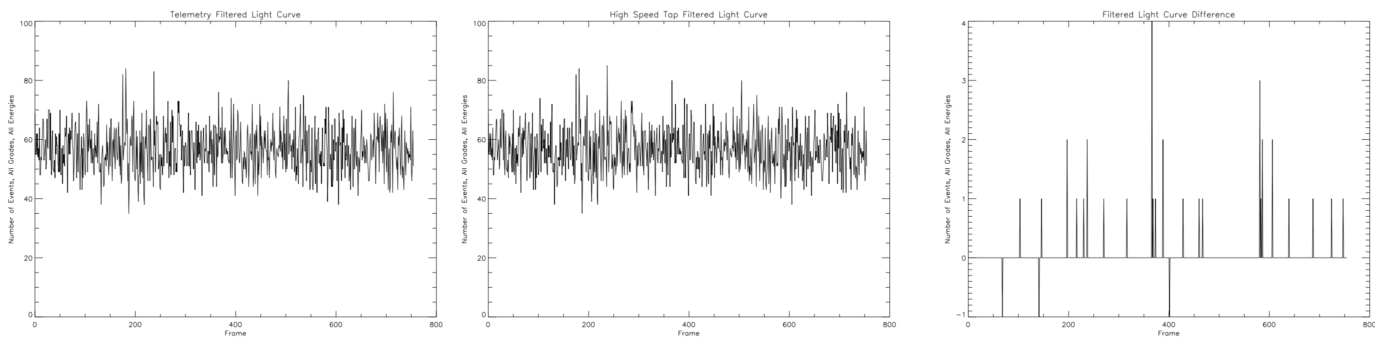

Figure 1.75: Telemetry, High Speed Tap, and Difference Light Curves

1.6.5.8 Position Comparison

Subtracting the event list images for the two files shows that there are 124 pixels for which the total number of events is different.

Ninety-six of the differences are due to split events which, because to differences in the biases or processing order, have a difference in the position of one row or column.

Table 1.32 is an example of an event found in the exposure taken at 22:45.558 GMT (frame 502 for the High Speed Tap, frame 5075 for the telemetry). Due to the 3 ADU difference in the bias levels, the peak of this split event was found at two different positions.

The remaining events which don't appear in both lists are events which are, due to the variations in the bias, either below the threshold, or are no longer the local maximum.

r/c	Telemetry				High Speed Tap				Difference			
	169	170	171	172	169	170	171	172	169	170	171	172
9		1	1	4	2	2	3		-2	-1	-2	+2
10		124	125	-4	2	127	126		+1	-3	-1	-3
11		65	96	-3	1	66	97		-2	-1	-1	+2

Table 1.32: Event Position Comparison

1.6.6 ACIS High Speed Tap Count Rates During XRCF Phase I: Towards Absolute Efficiency Measurements from XRCF Data

1.6.6.1 Purpose

The purpose of this section is to present the measured counting rate and inferred photon fluxes during XRCF phase I measurements.

Also presented is the ratio of ACIS detected counts (corrected for pileup and filter efficiencies) to the flux detected by the Beam Normalization Detector (corrected for source to detector distance). This information, combined with the absolute efficiency of the Beam Normalization Detector (which is not available to us at this time) can be used to determine the the absolute quantum efficiency of the ACIS CCDs.

1.6.6.2 Measurement Description

XRCF phase I was performed with the ACIS flight instrument, but without the HRMA or the gratings. The full ACIS focal plane was illuminated with X-rays from either the EIPS or the DCM.

ACIS was run in the full frame timed exposure mode, with a 3.34 second exposure time. During most science runs, six of the CCDs were read out simultaneously. During each science run, the high speed tap was cycled through each of the devices that was on. As the high speed tap was changed, so was the TRW ID.

There are two reasons why high speed tap data are used here in favor of telemetry data. Without the limitations of the telemetry, the entire full frames can be captured, not just the events from a small window. Also, because a single science run contains data from may TRW IDs, a time filter must be applied when comparing the telemetry data to the Beam Normalization Detector data. Using High Speed Tap data eliminates this complication.

The tables presented in this section identify the data used by science run number, not TRW ID. A single science run is all of the data taken between sending the "Start Run" and "Stop Run" commands to the ACIS instrument and often includes several TRW IDs.

Table 1.33 lists the relevant TRW IDs for the data used in this section.

Science Run	Energy	i0	i1	i2	i3	s0	s1	s2	s3	s4	s5
	eV	I-IAI-EA-	I-IAI-EA-	I-IAI-EA-	I-IAI-EA-	I-IAS-EA-	I-IAS-EA-	I-IAS-EA-	I-IAS-EA-	I-IAS-EA-	I-IAS-EA-
70 71	525	1.001	1.002	1.003	1.004	2.001	2.002	2.003	2.004	2.005	2.006
88 89	705	1.005	1.006	1.007	1.008	2.007	2.008	2.009	2.010	2.011	2.012A
111 112	1487	1.017	1.018	1.019	1.020	2.026	2.027	2.028	2.029	2.030	2.031
72 75	1740	1.009	1.010	1.011	1.012	2.013	2.014	2.015	2.016	2.017	2.018
107 108	2166	1.013	1.014	1.015	1.016	2.019	2.020	2.021	2.022	2.023	2.024
120 122 123	4509	1.121	1.122	1.123	1.124	2.131	2.132	2.133	2.134	2.135	2.136
77 78 83 84	6399	1.025	1.026	1.027	1.028	2.037	2.038	2.039	2.040	2.041	2.042
92 93	8040	1.029	1.030	1.031	1.032	2.043	2.044	2.045	2.046	2.047	2.048

Table 1.33: TRW IDs

1.6.6.3 Data Processing

Event finding was performed on each raw data frame with an event threshold of 38 ADU for the front illuminated devices and 20 ADU for the back illuminated devices. The split threshold was 13 ADU for all measurements. The event finding was performed using an IDL script which output an ARV format event list.

Each ARV format event list was then summarized using an IDL script. This IDL script fit a gaussian to the main peak of the spectrum. Only events in ACIS grade bit map 0x1d05 0x0047 0x0004 0x0047 0x1133 0x0003 0x1100 0x0000 0x1d04 0x0000 0x0004 0x0000 0x0000 0x0003 0x0000 0x0000 (ASCA grades 02346) were considered. Using the fit parameters, the position of the peak, width of the peak, and total number of counts under the peak are determined assuming the line response is Gaussian. All of these values are written to a text format file.

Finally, the text format summary files are read by another IDL script which uses the counts per frame versus energy to correct for pileup, the filter efficiency versus energy to correct for filter effects, and the CSR calculated s2 quantum efficiency. This IDL script also reads in a SSD 5 flux rate.

1.6.6.4 Results

The absolute flux at the ACIS filter in photons per second per centimeter squared is shown in Table 1.34. The statistical error of the flux rates presented is generally 0.1 percent, with a worse case of 0.5 percent.

The relative efficiencies of the ACIS flight devices compared to s2 are shown in Table 1.35.

Science Runs	Energy	i0	i1	i2	i3	s0	s1	s2	s3	s4	s5
70 71	525	18.1	18.3	18.2	17.3	18.6	26.2	18.9	24.6	18.1	18.0
88 89	705	23.7	23.3	23.5	23.8	23.6	40.0	24.4	39.9	25.7	23.8
111 112	1487	171.7	171.7	172.2	172.4	171.7	172.7	172.5	174.5	173.1	172.4
72 75	1740	39.5	39.6	39.8	39.7	39.6	41.4	39.5	41.7	39.6	39.3
107 108	2166	73.2	73.6	73.8	73.6	73.2	76.3	74.4	78.9	73.6	74.3
120 122 123	4509	64.7	66.0	65.0	65.9	76.8	68.6	74.0	75.1	70.8	69.3
77 78 83 84	6399	78.3	79.1	79.5	79.4	79.5	73.4	79.0	76.1	78.8	78.5
92 93	8040	242.9	244.4	240.4	245.7	254.1	230.9	246.4	233.2	243.4	247.8

Table 1.34: Estimated High Speed Tap Flux at ACIS Focal Plane Corrected for Pileup, Filter Efficiency, and CCD Efficiency in photons per second per centimeter squared in the line.

Science Runs	Energy	i0	i1	i2	i3	s0	s1	s2	s3	s4	s5
70 71	525	0.755	0.805	0.825	0.887	0.922	3.311	1.000	3.216	0.843	0.807
88 89	705	0.559	0.867	0.684	0.652	0.851	3.193	1.000	3.173	0.914	0.854
111 112	1487	0.967	0.949	0.962	0.972	0.978	1.076	1.000	1.161	0.984	0.975
72 75	1740	0.965	0.967	0.976	0.971	0.948	0.672	1.000	1.042	0.956	0.943
107 108	2166	0.944	0.957	0.970	0.958	0.964	1.282	1.000	1.328	0.975	0.964
120 122 123	4509	1.002	1.007	0.995	0.999	0.998	0.843	1.000	0.969	1.003	0.994
77 78 83 84	6399	0.949	0.950	0.957	0.954	0.951	0.604	1.000	0.750	0.992	0.976
92 93	8040	0.901	0.906	0.891	0.911	0.936	0.489	1.000	0.638	0.990	0.976

Table 1.35: High Speed Tap Based Quantum Efficiencies Relative to the s2 Detector

The ratio of ACIS counts to SSD 5 counts is shown in Table 1.36. The SSD 5 count rates used are from "flux_d3" column of ftp://es81-server1.msfc.nasa.gov/xrayastronomy/QE_energy_total.rdb, which was last updated August 13, 1997.

Science Runs	Energy	i0	i1	i2	i3	s0	s1	s2	s3	s4	s5
70 71	525	3.621	3.862	3.960	4.256	4.422	15.887	4.798	15.430	4.044	3.870
88 89	705	0.790	1.224	0.966	0.921	1.201	4.508	1.412	4.479	1.290	1.205
111 112	1487	0.977	0.958	0.972	0.982	0.988	1.087	1.010	1.173	0.994	0.985
72 75	1740	1.156	1.158	1.169	1.163	1.135	0.805	1.198	1.249	1.145	1.129
107 108	2166	0.782	0.793	0.804	0.794	0.799	1.063	0.829	1.100	0.808	0.799
120 122 123	4509	0.785	0.789	0.780	0.783	0.782	0.661	0.784	0.760	0.787	0.780
77 78 83 84	6399	0.792	0.793	0.799	0.796	0.793	0.504	0.834	0.626	0.828	0.815
92 93	8040	0.617	0.620	0.610	0.624	0.641	0.335	0.685	0.437	0.678	0.668

Table 1.36: ACIS Count Rate Divided by SSD 5 Count Rate

1.6.6.5 Warnings

The pileup correction applied to the data are based on CSR spectra, not XRCF spectra.